

# Structural basis of receptor usage by the engineered capsid AAV-PHP.eB

Seongmin Jang,<sup>1</sup> Hao K. Shen,<sup>2</sup> Xiaozhe Ding,<sup>1</sup> Timothy F. Miles,<sup>1</sup> and Viviana Gradinaru<sup>1</sup>

<sup>1</sup>Division of Biology and Biological Engineering, California Institute of Technology, Pasadena, CA 91125, USA; <sup>2</sup>Division of Chemistry and Chemical Engineering, California Institute of Technology, Pasadena, CA 91125, USA

**Adeno-associated virus serotype 9 (AAV9) is a promising gene therapy vector for treating neurodegenerative diseases due to its ability to penetrate the blood-brain barrier. PHP.eB was engineered from AAV9 by insertion of a 7-amino acid peptide and point mutation of neighboring residues, thereby enhancing potency in the central nervous system. Here, we report a 2.24-Å resolution cryo-electron microscopy structure of PHP.eB, revealing conformational differences from other 7-mer insertion capsid variants. In PHP.eB, the 7-mer loop adopts a bent conformation, mediated by an interaction between engineered lysine and aspartate residues. Further, we identify PKD2 as the main AAV receptor (AAVR) domain recognizing both AAV9 and PHP.eB and find that the PHP.eB 7-mer partially destabilizes this interaction. Analysis of previously reported AAV structures together with our pull-down data demonstrate that the 7-mer topology determined by the lysine-aspartate interaction dictates AAVR binding strength. Our results suggest that PHP.eB's altered tropism may arise from both an additional interaction with LY6A and weakening of its AAVR interaction. Changing the insertion length, but not sequence, modifies PKD2 binding affinity, suggesting that a steric clash impedes AAVR binding. This research suggests improved library designs for future AAV selections to identify non-LY6A-dependent vectors and modulate AAVR interaction strength.**

## INTRODUCTION

Adeno-associated virus (AAV) is a member of the *Parvoviridae* that comprises an icosahedral 60-protein capsid packaging a single-stranded DNA (ssDNA) genome.<sup>1,2</sup> Recombinant AAV (rAAV) vectors offer a promising delivery vehicle for the gene therapy field due to their infectivity toward both dividing and non-dividing cells and their low pathogenicity.<sup>3–5</sup> In particular, the AAV9 serotype, which can penetrate the blood-brain barrier (BBB) and transduce the central nervous system (CNS), is a focus of intense study for the treatment of neurodegenerative diseases.<sup>6,7</sup> However, AAV9 has a broad tropism, targeting non-neuronal as well as neuronal cells, which has limited its application as a CNS-targeting vector.

Our group and others have used directed evolution to create multiple rAAV vectors with enhanced and selective tropism toward the CNS.<sup>8–10</sup> Of particular interest, the AAV-PHP.B (PHP.B) and

AAV-PHP.eB (PHP.eB) variants of AAV9 show highly CNS-enhanced tropism and have been widely adopted both in basic research and preclinical gene therapy studies.<sup>8,11</sup> PHP.B was evolved by inserting seven randomized amino acids, TLAVPFK, between residues 588 and 589 of viral protein 1 (VP1), which are at the outermost tip of the capsid's protruding VR-VIII loop. PHP.eB was created by adding two point mutations at residues 587 (A587D) and 588 (Q588G) to PHP.B, further enhancing tropism toward the CNS.

The infection mechanism of AAV is still poorly understood, although a few key vertebrate recognition factors have been identified. *N*-linked glycans, in particular those with terminal galactosyl residues, have been shown to be the primary receptors of AAV9.<sup>12–15</sup> AAV receptor (AAVR) is another essential factor for AAV infection in most, but not all, known serotypes.<sup>16–18</sup> AAVR contains an array of five immunoglobulin (Ig)-like polycystic kidney disease domains (PKD1–5) that share a conserved  $\beta$ -barrel structure but present different residues on their surface so that each PKD domain forms distinct interactions with different AAV serotypes.<sup>16,19–23</sup> AAV1, AAV2, and AAV8 interact with the PKD2 domain, while AAV5 interacts with PKD1. Interestingly, AAV2 can attach to the cell surface without AAVR but cannot transduce cells, indicating that AAVR may act as a trafficking factor rather than simply a binding platform.<sup>18</sup> AAVR is also known to play a key role in AAV9 and PHP.eB infection *in vivo*,<sup>16,19</sup> but the relevant interacting domain has not been identified. Recently, several groups reported that PHP.B and PHP.eB directly bind to lymphocyte activation protein 6A (LY6A), a glycosylphosphatidylinositol (GPI)-anchored protein on brain macrovascular endothelial cells that likely serves as the receptor for BBB penetration and CNS infection of these engineered capsids.<sup>24–26</sup>

In this study, we present the cryo-electron microscopy (cryo-EM) structure of PHP.eB and analyze the function of the 7-mer amino acid peptide insertion by comparing our structure with those of other natural and engineered capsids. Interestingly, we find that the 7-mer loops exhibit different rigidity and conformation depending on neighboring residues in the VR-VIII loop. In particular, we find

Received 29 April 2022; accepted 15 July 2022;  
<https://doi.org/10.1016/j.omtm.2022.07.011>

**Correspondence:** Viviana Gradinaru, PhD, Division of Biology and Biological Engineering, California Institute of Technology, Pasadena, CA 91125, USA.  
**E-mail:** [viviana@caltech.edu](mailto:viviana@caltech.edu)



that lysine of the 7-mer interacts with a nearby aspartate, replacing the A587 in the wild type to form a lysine lever that contributes to the conformation of the VR-VIII protrusion. Pull-down assays of recombinant AAVs (rAAVs) and receptors reveal that only the PKD2 domain strongly interacts with both AAV9 and PHP.eB. Finally, we find that the 7-mer conformation translates into differences in receptor usage, modifying binding strength toward PKD2 and LY6A binding availability. Together, our results rationalize how 7-mer modifications can change receptor affinity and selectivity and provide hints for further rational design of rAAVs.

## RESULTS

### Cryo-EM determination of AAV-PHP.eB capsid structure

To investigate the CNS-enhanced tropism of PHP.eB, we solved a high-resolution cryo-EM structure of PHP.eB by single-particle reconstruction (Figure 1A). The resolution of 2.24 Å, estimated by gold-standard Fourier shell correlation (FSC) cutoff at 0.143 (Figure S1; Table S1), was sufficient to allow us to accurately refine an atomic model of both backbone and side chains using a previously determined crystal structure of the parent AAV9 (Protein Data Bank [PDB]: 3UX1) as a template.<sup>27</sup> The resulting model of PHP.eB shows an ordered structure from residues 219 to 743 (Figures 1B and 1C).

At a high contour level, the VR-VIII protrusion shows relatively weak electron density, indicating that this part might be more flexible than other parts of the capsid. However, at a lower contour level of  $\sigma \approx 2$ , we observed electron density from the 7-mer peptide at the outermost portions of the VR-VIII protrusions (Figure 1C). The electron density forms a partial loop that is disconnected in the middle (Figure 1C). On one side, electron density consistent with two residues extends from the C terminus of D587, while on the other side, another two residues' worth of electron density extends from the N terminus of the lysine in the 7-mer. This suggests that the VR-VIII 7-mer protrusion, while not highly rigid, exhibits some preferred structure.

We manually built the model of the 7-mer amino acids and two mutated residues (<sub>587</sub>DGTLAVPFK<sub>7</sub>) of PHP.eB into one of the monomer maps and refined the model with PHENIX (Figure 1C).<sup>28</sup> We denote the threonine, leucine, alanine, valine, proline, phenylalanine, and lysine in the 7-mer as T1', L2', A3', V4', P5', F6', and K7', respectively. Despite the overall flexibility of the VR-VIII protrusion, we could confidently place residues D587, G588, and K7'. For residues T1', P5', and F6', it was difficult to ascertain the conformation of side chains, so we located them based on the rotamer suggestion and real-space refinement functions of Coot and PHENIX,<sup>28,29</sup> which revealed that the side chains of both P5' and F6' pointed toward the capsid surface. A patch of three hydrophobic residues, L2', A3', and V4' (<sub>2</sub>LAV<sub>4</sub>), was fully disordered, as expected given its highly solvent-exposed position at the outermost tip of the loop. It is very likely that the conformational heterogeneity we observed in T1' and P5' is an effect of the disordered nature of these neighboring hydrophobic residues.

To examine any structural information lost by imposing icosahedral symmetry (I1) during averaging, we also determined the symmetry-

free cryo-EM structure of PHP.eB (Figure S2; Table S1). Even without icosahedral symmetry, the resolution of the reconstruction was high: 2.90 Å. Looking at the insertion loop in the VR-VIII protrusion, we found that approximately two-thirds of the monomers displayed a partial loop structure as observed in the I1 symmetry reconstruction, indicating that this 7-mer structure might be the most stable conformation. As in the I1 symmetry structure, <sub>2</sub>LAV<sub>4</sub> was disordered in all monomers. These residues are not highly conserved among BBB-crossing AAV9 variants, suggesting that this patch does not form a biochemical or structural motif (Figure 1D).

### The bent 7-mer conformation is a unique feature of PHP.eB conferred by an electrostatic lysine-aspartate interaction

The high resolution of our PHP.eB structure revealed that the acidic residue D587 is positioned to interact with K7' on the opposite side of the 7-mer loop (Figure 2A). The distance between this residue pair is short enough for both hydrogen bonding and electrostatic interaction. This interaction seems to hold two sides of the loop together, limiting the flexibility of the 7-mer. Notably, this interaction is only possible due to a mutation, A587D, introduced in the iterative engineering of PHP.B into PHP.eB. To investigate the effect of this molecular interaction, we superimposed our PHP.eB monomer structure on other, published structures of AAVs: AAV9, PHP.B, and AAV1-PHP.B, which is a variant of the AAV1 serotype containing the same VR-VIII 7-mer insertion as in PHP.eB (Figures 2B and 2C).<sup>15,27,30</sup> Most of the ordered regions were similar, especially in AAV9 variants; AAV9, PHP.B, and PHP.eB shared almost identical structures in both highly ordered regions and flexible loops. Interestingly, however, we found that the bent 7-mer is a unique feature of PHP.eB, lacking even in other variants with an identical 7-mer insertion (Figures 2C and 2D).

Looking for the basis of this difference, we found that the angle of the loop correlates with the orientation of the lysine in the 7-mer (Figure 2D).<sup>30</sup> In PHP.eB, the interaction we observed between D587 and K7' appears to introduce an inward tension on the loop that could bend the 7-mer tip downward (Figure 2D, top right). In AAV1-PHP.B, however, K7' is instead positioned to interact with D590, pulling the 7-mer upward (Figure 2D, bottom right). In PHP.B, K7' does not seem to interact with any nearby residues, likely explaining the flexibility that washes out the electron density of the 7-mer (Figure 2D, bottom left). These results indicate that K7' works as a lysine lever that controls the conformation of the 7-mer tip and suggest an idea for rational design of the structure through strategic positioning of an acidic residue close to this lysine lever. Our results also suggest an explanation for why PHP.eB exhibits much stronger CNS tropism than PHP.B despite differing in only two residues: the interaction between D587 and K7' of PHP.eB, by limiting the flexibility of the 7-mer, may keep it in a structural conformation favored by receptors on the BBB or CNS cells.

### AAV9 and PHP.eB interact with the PKD2 domain of AAVR, and the 7-mer orientation predicts the AAVR binding strength

AAVR is a direct receptor for multiple AAVs, including AAV9, and is essential for efficient cell infection.<sup>16,17</sup> After determining the

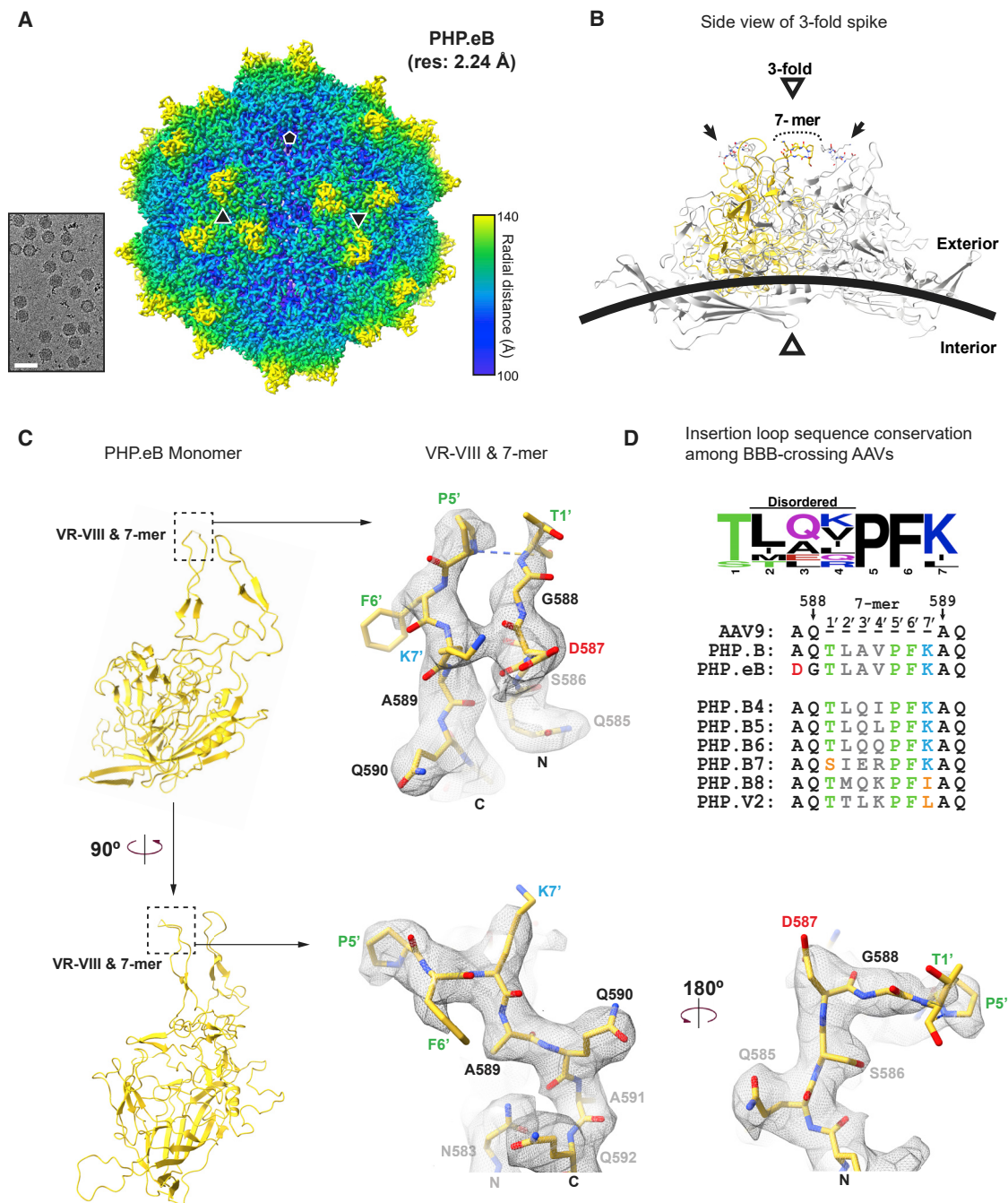


**Figure 1. High-resolution cryo-EM structure of AAV-PHP.eB**

(A) Representative micrograph and resulting single-particle cryo-EM reconstruction of AAV-PHP.eB (PHP.eB). Color indicates the distance from the capsid center (purple: 100 Å; yellow: 140 Å). Triangles and pentagon indicate the icosahedral 3- and 5-fold axes, respectively. Scale bar: 50 nm. (B) Model of 3-fold spike trimer built using the PHP.eB monomer structure. One of the monomers is colored yellow. The other two monomers are colored gray. Dashed arch and black arrows indicate the 7-mers of each monomer. (C) Atomic model of PHP.eB monomer (left), and cryo-EM map with fitted atomic model of the 7-mer and two point mutations in the VR-VIII loop of PHP.eB (right). Cryo-EM map is contoured at a level of  $\sigma \approx 2$ . (D) Sequences of AAV-PHP variants' 7-mer peptides inserted between residues 588 and 589 of AAV9. Conserved residues are colored green. Unique residues are colored orange. Partially conserved residues are colored gray. Basic residues are colored blue. Acidic residue is colored red. Residue frequency for just the 7-mer is shown above. Size of letter represents prevalence, and color represents properties of residues.

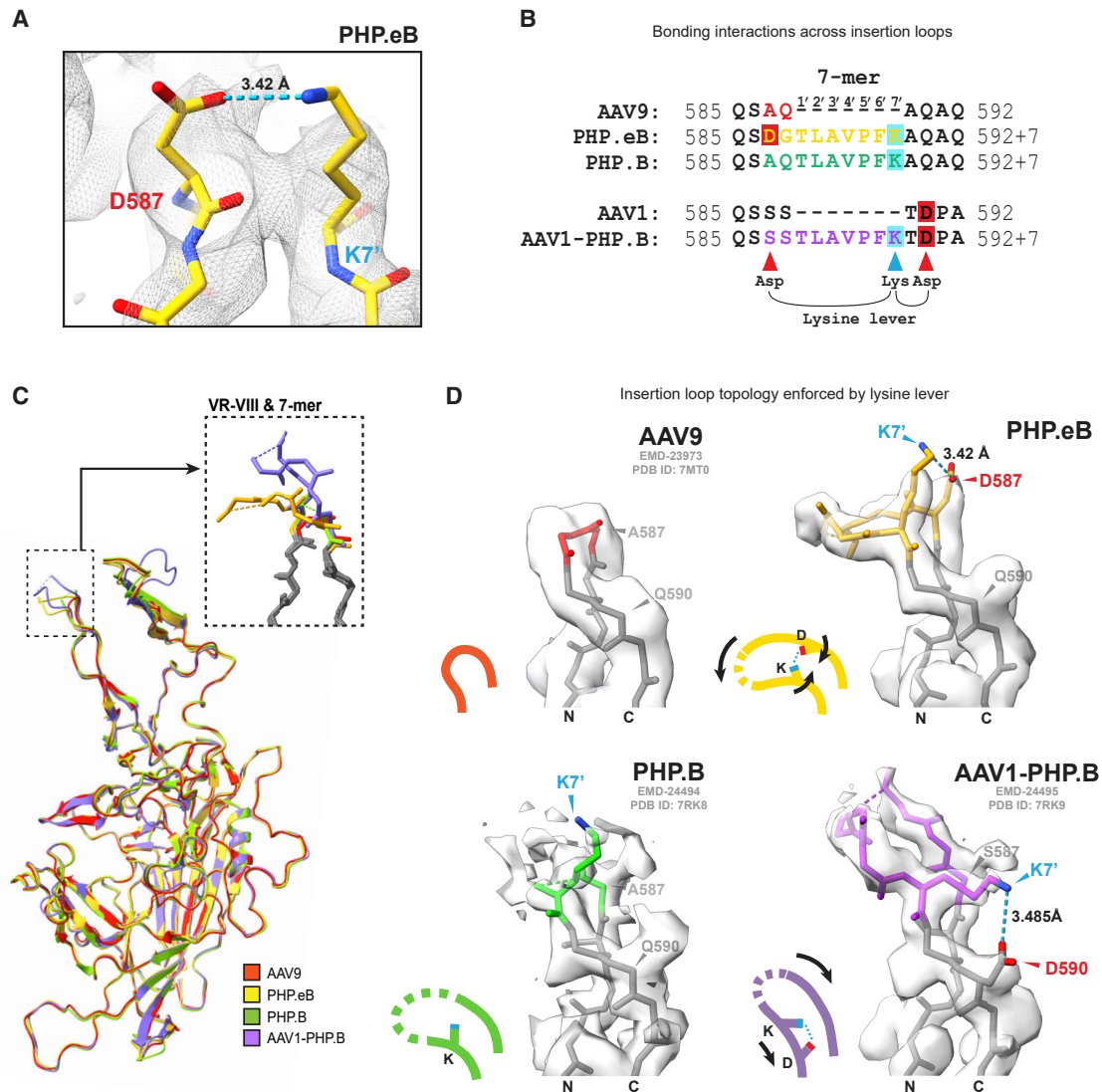


**Figure 2. Lysine-aspartate interaction dictates 7-mer loop topology**

(A) Interaction site between D587 and K7' of PHP.eB. (B) Comparison of 7-mer sequences of AAV9 variants (top) and AAV1 variants (bottom). Residues 587 and 588 and the 7-mer are colored by variant according to the color code shown in (C). Aspartates are indicated by red boxes and red arrowheads. Lysines are indicated by blue boxes and a blue arrowhead. Lysine lever pairs are indicated with arches. (C) Superimposition of atomic models of AAV9 (PDB: 7MT0), PHP.eB (this study), AAV-PHP.B (PDB: 7RK8), and AAV1-PHP.B (PDB: 7RK9). Detail of the outermost tip of VR-VIII (dashed box) is enlarged in the inset. In the inset, residues 587 and 588 and the 7-mer are colored according to variant, and other regions are colored gray. (D) Cryo-EM maps with atomic models of the 7-mer insertion region of AAV9 (PDB: 7MT0, EMD: 23973), PHP.eB (this study), AAV-PHP.B (PDB: 7RK8, EMD: 24494), and AAV1-PHP.B (PDB: 7RK9, EMD: 24495). Residues 587 and 588 and the 7-mer are colored by variant according to the color code in (C), and other regions are colored gray. Cartoons illustrate topology.

structure of PHP.eB, we conducted pull-down assays to screen which of the five domains of AAVR, PKD1, 2, 3, 4, and/or 5, mediates interaction with AAV9 and PHP.eB. We immobilized each polyhistidine (6xHis)-tagged PKD on Ni-NTA resin and added AAV9 or PHP.eB as a prey to analyze the interaction (Figure 3A). As a negative control, we used 6xHis-tagged IgG-Fc (His-Fc). The results revealed that both AAV9 and PHP.eB bind to the PKD2 domain of AAVR and not significantly to any other PKD (Fig-

ure 3B). This result is consistent with AAV9's sequence and structural conservation with AAV1 and AAV2; AAV1 and AAV2 are known to interact with PKD2 in the same 3-fold conformation.<sup>20–22</sup> We generated a phylogenetic tree of the sequences of the capsid-forming VP3 and found that AAV9 clusters with AAV1, AAV2, and AAV8, all of which interact with the PKD2 domain of AAVR, while AAV5, the only known PKD1 interactor, is highly divergent (Figure S3A).<sup>19</sup> In addition, the loop regions VR-I, VR-III,

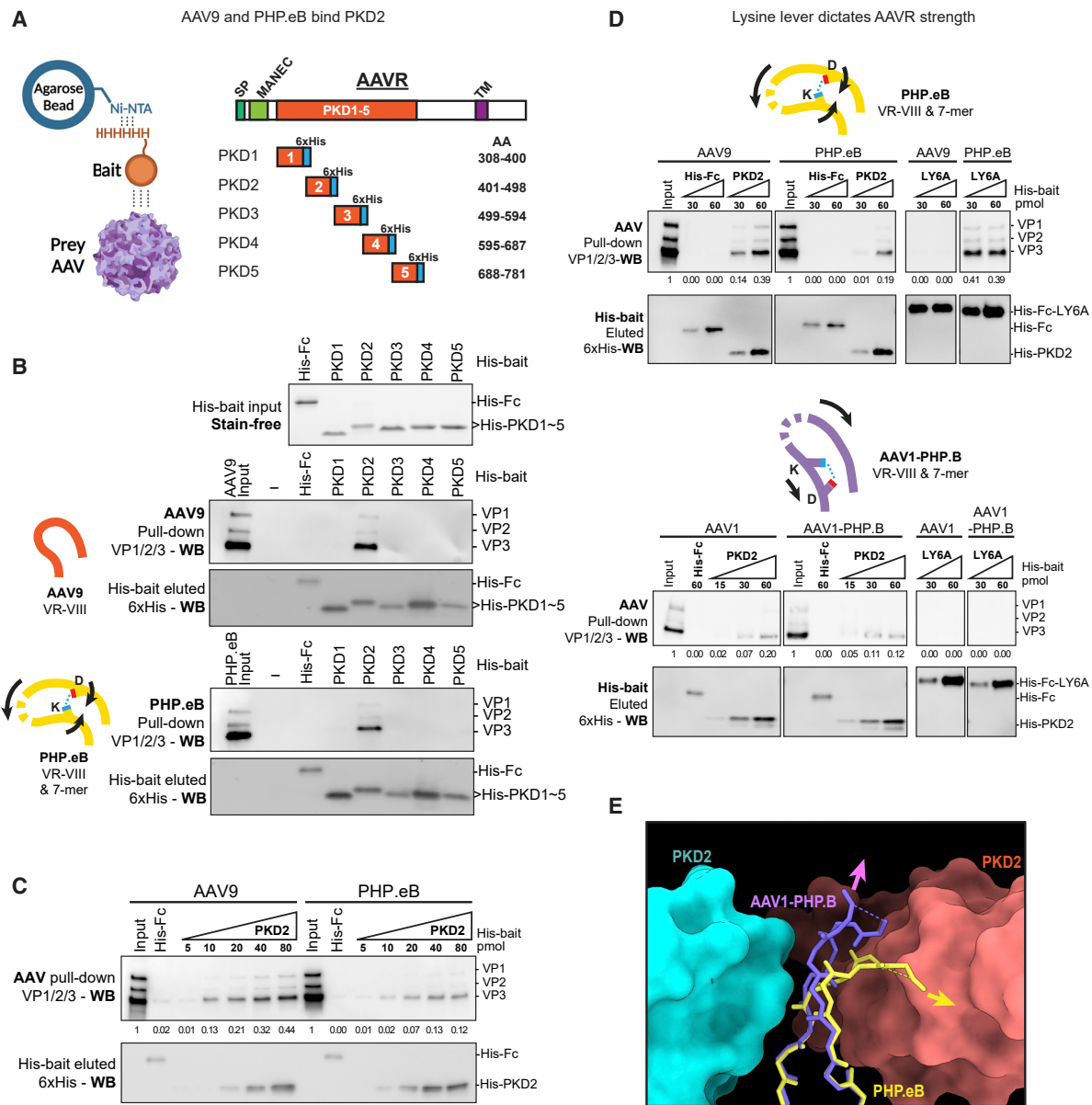


**Figure 3. AAV9 and PHP.eB bind PKD2, and the lysine lever dictates binding strength**

(A) Left: experimental scheme of pull-down assay. 6x-His-tagged bait proteins are immobilized on Ni-NTA agarose resin. Only AAVs bound to the bait are fished out from the mixture. AAVs that cannot recognize the bait are washed out. Right: domain map of AAVR and design of 6xHis-tagged single PKD constructs for pull-down assays. (B–D) Pull-down assays of rAAVs with single PKD domains (6xHis-PKD1–5) or LY6A. (B, top) 6xHis-tagged single PKD domains and 6xHis-tagged Fc. (B, middle and bottom) AAV9 and PHP.eB with 6xHis-PKD1–5. (C) AAV9 and PHP.eB with a gradient of increasing concentration of 6xHis-PKD2. (D, top) AAV9 and PHP.eB with 6xHis-PKD2 and 6xHis-LY6A. (D, bottom) AAV1 and AAV1-PHP.B with 6xHis-PKD2 and 6xHis-LY6A. 0.05 pmol AAV was used for each pull-down. All AAV pull-downs were analyzed by western blotting with antibody against VP1/2/3. Half of each pull-down was run on a separate gel and analyzed by western blotting with an antibody against the 6xHis-tag. The same amount of AAV used for each pull-down was loaded in the first lane (“input”). His-Fc was used as a control. VP3 band intensities were normalized to the input of each set and are presented below each lane. Note that blocks of lanes have been reordered for display. (E) 7-mer PHP.eB (yellow, this study) and AAV1-PHP.B (purple, PDB: 7RK9) atomic models superimposed onto the trimeric AAV1-PKD2 complex structure (PDB: 6JCQ). Two PKD2s are colored cyan and red. Arrows indicate the protrusion direction of each 7-mer.

VR-VI, and VR-VIII, which are known to bind PKD2, show conservation of both sequence and structure between AAV9, PHP.eB, AAV1, and AAV2 (Figure S3B).<sup>20–22,27</sup> Together, these results

strongly suggest that both AAV9 and PHP.eB require PKD2 to transduce cells and likely do so through a similar interaction interface as other PKD2-binding serotypes.

Interestingly, in our pull-down assays, we observed that His-PKD2 consistently pulled down less PHP.eB than AAV9, suggesting that the binding affinity of PKD2 for PHP.eB might be weaker than for AAV9. To confirm this, we gradually increased the amount of His-PKD2 bait and detected the corresponding amount of AAV pulled down (Figure 3C). Indeed, the amount of capsid pulled down was consistently less for PHP.eB than for AAV9 across a 16-fold concentration gradient of PKD2, indicating that PKD2 does bind PHP.eB more weakly than AAV9.

LY6A was recently identified as a direct and critical interaction partner of PHP.eB.<sup>24–26</sup> We therefore performed pull-down assays of AAV9 and PHP.eB with 6xHis-tagged LY6A as a bait (Figure 3D, top). We found that LY6A pulled down PHP.eB even more efficiently than PKD2 did. By contrast, LY6A did not detectably capture any AAV9 capsids, revealing significantly different receptor selectivity for AAV9 and PHP.eB. Our results suggest that <sub>587</sub>DGTLAVPFK<sub>7</sub> offers a binding platform for LY6A receptors while simultaneously destabilizing binding with AAVR-PKD2.

To test whether the topology of the 7-mer impacts AAVR-PKD2 binding strength and receptor selectivity, we conducted similar pull-down assays with AAV1 and AAV1-PHP.B, which has a different 7-mer conformation than PHP.eB (Figure 3D, bottom). Interestingly, for AAV1-PHP.B, we did not find any significant difference in PKD2 binding of AAV1-PHP.B compared with AAV1, indicating that the 7-mer in AAV1-PHP.B does not alter the PKD2 binding strength. Neither AAV1 nor AAV1-PHP.B showed any binding to LY6A, as previously reported,<sup>30</sup> suggesting that the different conformation of the 7-mer in AAV1-PHP.B is not favorable for LY6A.

Based on our pull-down assays, VP3 phylogenetic analysis, and structural comparison of PKD2 interaction sites, we assumed that AAV9 and PHP.eB would share the same PKD2-interacting 3-fold conformation as AAV1 and AAV2.<sup>20–22</sup> Thus, we superimposed our new PHP.eB model and the previously reported AAV1-PHP.B model onto a previously reported AAV1-PKD2 trimer complex structure (PDB: 6JCQ) (Figure 3E).<sup>20</sup> The location of the VR-VIII protrusion, including the 7-mer peptide, in the tight interface between two neighboring PKD2 domains suggests that the bulky 7-mer may cause a steric clash with PKD2. The bent angle of the PHP.eB 7-mer appears to enhance this clash with PKD2, which would explain its weaker binding. By contrast, in AAV1-PHP.B, the upright conformation of the 7-mer loop positioned it to extend through the channel without clashing, explaining the similarity of its PKD2 binding affinity to AAV1 in pull-down assays.

We next compared the PKD2 binding affinities of PHP.eB and PHP.B (Figure S4A). Our pull-down assays showed that AAV-PHP.B was captured less efficiently than PHP.eB. To further understand the difference between PHP.B and PHP.eB, we modeled the missing parts of the VR-VIII loops in PHP.B and PHP.eB using RosettaRemodel (Figure S4C).<sup>31</sup> Structural modeling resulted in divergent poses of the 7-mer in both PHP.B and PHP.eB, consistent with the loss of electron

densities observed in cryo-EM structures (Figure 2D). A large fluctuation in predicted structures around F6'-A589 of PHP.B, near the PKD2 interaction site (Figure S3B), suggests that the hydrophobic phenylalanine in this solvent-exposed position destabilizes the loop structure (Figure S4C). Among the top ten PHP.eB 7-mer models, four models (colored red, orange, and yellow) showed a similar structure as our cryo-EM reconstruction, while the other models (colored purple, blue, and green) diverged around F6', similar to the PHP.B structure (Figure S4C). These models suggest that the lysine lever in PHP.eB limits the mobility of F6' and A589, thereby reducing the structural instability of the 7-mer.

### The flexibility and size of a peptide insertion in the VR-VIII protrusion can alter the AAVR binding affinities of engineered rAAVs

To further test the hypothesis that 7-mer topology impacts AAVR-PKD2 binding affinity, we designed new PHP.eB variants, TLAV(-), TLAV(×2), and TLAV to AGAG, which have a shorter peptide, a longer peptide, and smaller residues in the peptide, respectively (Figures 4A and 4B). We then conducted pull-down assays to compare the amount of each new variant captured by PKD2 with wild-type AAV9 and PHP.eB (Figures 4C–4E). As expected, TLAV(×2) lost nearly all PKD2 binding affinity, consistent with the longer VR-VIII protrusion causing more steric hindrance in the PKD2 gap (Figure 4C). In contrast, TLAV(-) recovered PKD2 binding affinity to a level similar to wild-type AAV9 (Figure 4D). For the TLAV to AGAG construct, we observed no obvious change in binding compared with PHP.eB, indicating that PKD2 recognition is influenced more by the length of the  $\alpha$ -carbon backbone than by the size or biochemical properties of residue side chains (Figure 4E).

We also designed a PHP.eB variant, eB-flip, which has a reversed 7-mer sequence (<sub>1</sub>-KFPVALT<sub>7</sub>), which we reasoned should transform the 7-mer structure upward (Figure 4B). We then conducted pull-down assays to test whether reversing the bending direction can recover PKD2 binding affinity (Figure 4F). However, eB-flip showed a similar PKD2 binding affinity to PHP.eB, suggesting that this dramatic change might modify the topological and biochemical properties of the loop, obscuring the effect of the different  $\alpha$ -carbon backbone conformation.

### <sub>5</sub>PFK<sub>7</sub> in the 7-mer is an essential motif required for LY6A recognition

We next tested if the newly designed PHP.eB variants still possess LY6A binding affinity. We conducted pull-down assays with PHP.eB variants (TLAV(×2), TLAV(-), TLAV to AGAG, eB-flip) and compared the amount of AAV captured by 6xHis-tagged LY6A (Figure 5). Surprisingly, only TLAV(-), which has the shortest peptide, could bind LY6A (Figure 5B), while the other variants completely lost LY6A binding affinity (Figures 5A, 5C, and 5D). This result indicates that of the 7-mer residues, P5', F6', and K7' (<sub>5</sub>PFK<sub>7</sub>) alone are sufficient for recognizing LY6A. The fact that all other PHP.eB variants lost their LY6A binding indicates that LY6A binding is more dependent on 7-mer conformation than PKD2 binding, which was

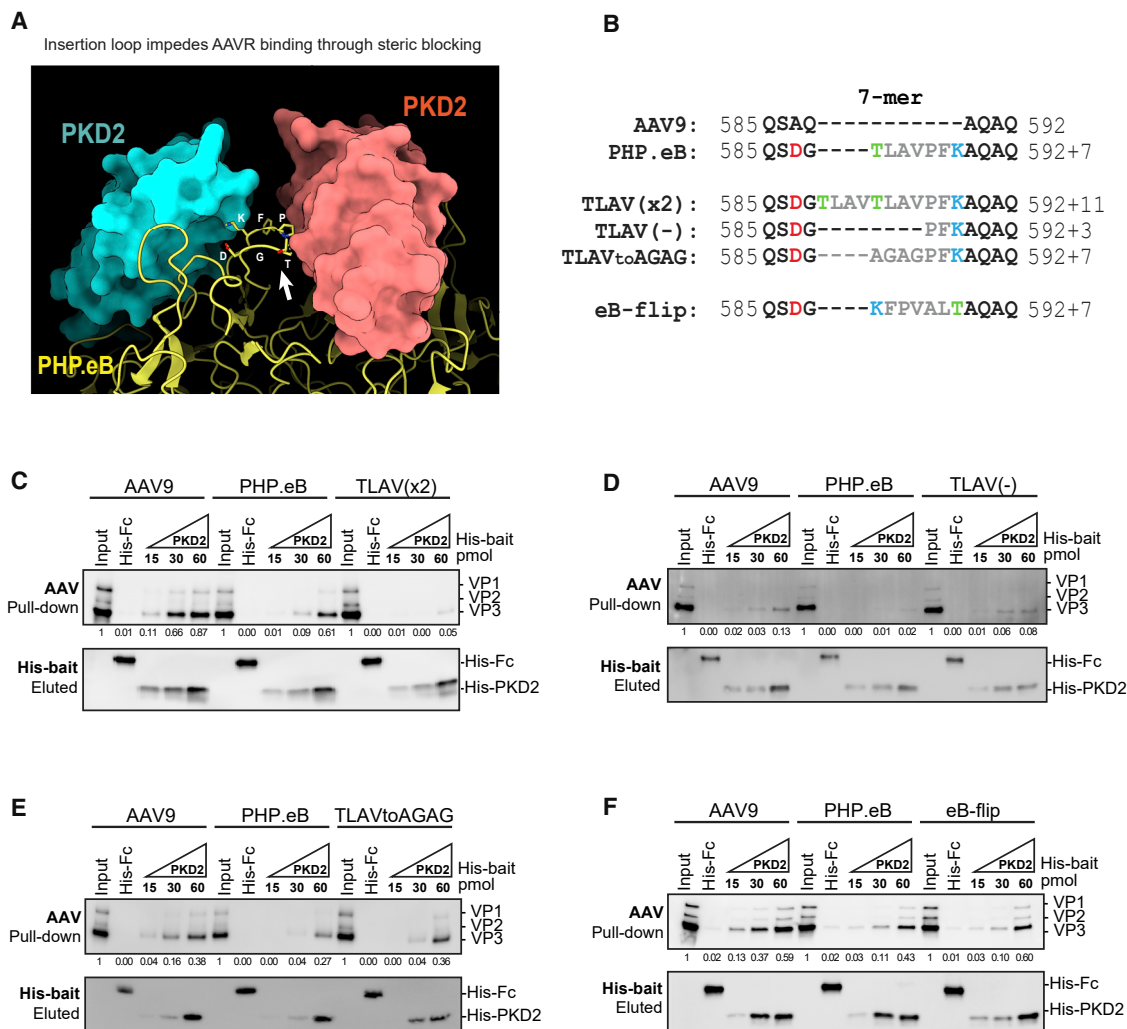


**Figure 4. Modification of the loop insertion can alter AAV-PKD2 binding strength**

(A) PHP.eB 7-mer atomic model superimposed onto the trimeric AAV1-PKD2 complex structure (PDB: 6JJCQ). PHP.eB is colored yellow. The white arrow indicates the PHP.eB 7-mer. Two PKD2s are colored cyan and red. The third PKD2 and the AAV2 trimer are not shown. (B) Sequences of modified 7-mers. Hydrophobic residues are colored gray. Aspartates are colored red. Lysines are colored blue. The first residue of the 7-mer is colored green. (C–E) Pull-down assays of modified AAVs, including the extended 7-mer TLAV(x2) (C); the shortened 7-mer TLAV(-) (D); the smaller-residue 7-mer TLAV to AGAG (E); and the reversed 7-mer eB-flip (F). 0.05, 0.01, 0.05, and 0.05 pmol AAV were used for each pull-down in (C)–(F), respectively. AAV pull-downs were analyzed by western blotting with antibody against VP1/2/3. Half of each pull-down was run on a separate gel and analyzed by western blotting with an antibody against the 6xHis-tag. The same amount of AAV used for each pull-down was loaded in the first lane (“input”). His-Fc was used as a control. VP3 band intensities were normalized to the input of each set and are presented below each lane.

never totally lost in the same PHP.eB variants (Figure 4). We also compared the LY6A binding affinity of PHP.B with PHP.eB and found it to be weaker (Figure S4B), as expected if the unstable VR-VIII structure of PHP.B impedes LY6A binding as it does for PKD2 (Figures S4A and S4C).

## DISCUSSION

PHP.eB has been widely adopted in the fields of neuroscience<sup>32–36</sup> and preclinical gene therapy<sup>37–42</sup> for its ability to penetrate the BBB, but the molecular basis of this behavior is poorly understood. Here, we determined a 2.24-Å resolution structure of PHP.eB showing that the in-

serted 7-mer of PHP.eB has higher flexibility than the rest of the capsid surface but that the two neighboring mutated residues D587 and G588, distinguishing PHP.eB from PHP.B, limit this mobility. Specifically, we find that K7' of the 7-mer acts as a lever for the VR-VIII loop, pairing with a nearby aspartate, either D587 in PHP.eB or D590 in AAV1-PHP.B, to control the angle of the protrusion. This suggests a possible strategy for further improving viral tropism by engineering the position and nature of the aspartate-lysine pair.

Previous *in vivo* studies showed that AAVR is essential for AAV9 and PHP.eB transduction of the mouse CNS,<sup>24</sup> and LY6A was recently

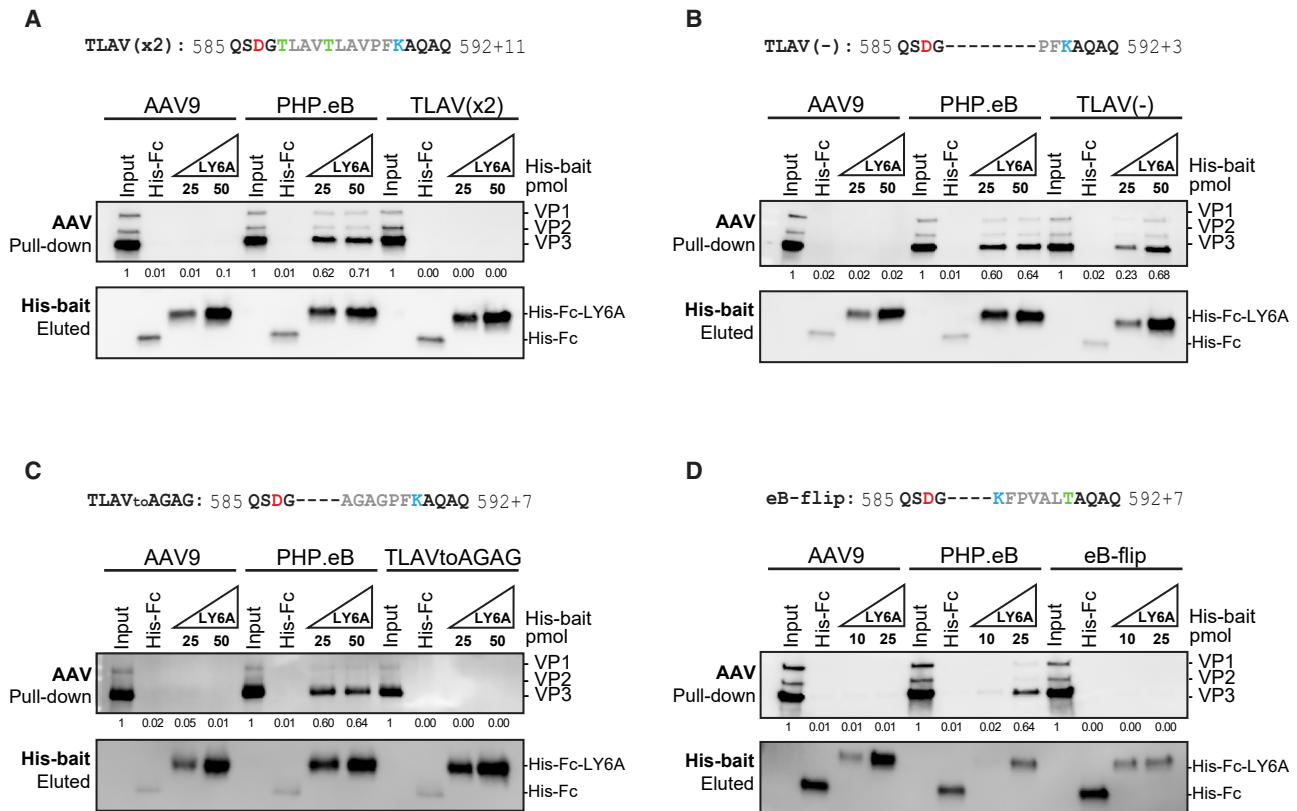


**Figure 5.**  ${}_{5}\text{PFK}_{7}$  in the 7-mer is an essential motif for binding LY6A

(A–D) Pull-down assays of modified AAVs, including the extended 7-mer TLAV( $\times 2$ ) (A); the shortened 7-mer TLAV(–) (B); the smaller-residue 7-mer TLAV to AGAG (C); and the reversed 7-mer eB-flip (D). 0.05 pmol AAV was used for each pull-down. All AAV pull-downs were analyzed by western blotting with antibody against VP1/2/3. Half of each pull-down was run on a separate gel and analyzed by western blotting with an antibody against the 6xHis tag. The same amount of AAV used for each pull-down was loaded in the first lane (“input”). His-Fc was used as a control. VP3 band intensities were normalized to the input of each set and are presented below each lane.

identified as a critical murine receptor for PHP.eB transduction.<sup>24–26</sup> Here, we find that the PKD2 domain of AAVR is the main receptor for AAV9 and PHP.eB *in vitro* and that PHP.eB shows relatively weaker binding affinity for PKD2 and higher affinity for LY6A than AAV9. This difference suggests that the 7-mer insertion may not only play a role in binding to new receptors (LY6A) but may also modify the recognition of existing receptors (AAVR-PKD2). One possible scenario is that while PHP.eB still requires AAVR for cell infection, its relatively unstable AAVR binding reduces infectivity, an effect compensated for, either directly or indirectly, by LY6A. PHP.eB could therefore stably bind cell membranes presenting LY6A, explaining the improved neurotropism of PHP.eB. Further biophysical and *in vivo* studies are needed to test this idea and determine the actual molecular mechanism.

We also show that the conformation of the 7-mer may impact AAVR binding strength *in vitro*. PHP.eB, AAV1-PHP.B, and PHP.B have different topologies of the 7-mer: bent downward, pulled upward, and disordered, respectively. PHP.eB and PHP.B show much weaker PKD2 binding than AAV9, while AAV1-PHP.B shows no significant

difference from AAV1. Our structural comparison and modeling suggest that the bent-downward or disordered structure of the 7-mer in PHP.eB and PHP.B, respectively, might destabilize PKD2 binding, while the upright 7-mer in AAV1-PHP.B avoids steric clashes with PKD2. Further, PHP.B shows even weaker PKD2 binding than PHP.eB. Our loop modeling results suggest that the lysine lever in PHP.eB may stabilize and narrow the 7-mer by limiting the mobility of hydrophobic alanine and phenylalanine and thereby reduce the steric hindrance against PKD2 interaction. As reported before, AAV1-PHP.B did not show any binding affinity toward LY6A, which is surprising because it contains the same 7-mer at the tip of the VR-VIII loop.<sup>30</sup> A different 7-mer conformation might explain why AAV1-PHP.B is not favored by LY6A. A previous study reported that replacing most of the VR-VIII loop in AAV1 with that of PHP.eB allowed it to interact with LY6A.<sup>30</sup> This replacement relocates an aspartate from AA590 to AA587 and therefore might switch the lysine lever so that the 7-mer adopts a conformation favorable for LY6A. Further structural and biophysical experiments will be required to fully understand the correlation between 7-mer conformation and AAVR selectivity.

Our structural comparison suggests an explanation for the weakened binding of PHP.eB to AAVR-PKD2: the 7-mer peptide insertion induces steric stress between neighboring PKD2s on 3-fold spikes. Informed by this analysis, we were able to successfully control the binding affinity of the PHP.eB capsid for PKD2 by changing the length of the insertion peptide. Duplicating or removing the most labile region of the 7-mer  $_1\text{TLAV}_4$  abrogated or strengthened PKD2 binding, respectively. Interestingly, replacing the hydrophobic residues  $_1\text{TLAV}_4$  with  $_1\text{AGAG}_4$  did not significantly change PKD2 binding. In the directed evolution that yielded the PHP.eB capsid, these residues were not highly conserved among selected variants, suggesting, with our results here, that the conformation, and not the biochemistry, of the  $_1\text{TLAV}_4$  patch is important for receptor binding. Further, we identified  $_5\text{PFK}_7$  as an essential motif in the PHP.eB 7-mer for binding LY6A. Contrary to  $_1\text{TLAV}_4$ ,  $_5\text{PFK}_7$  is highly conserved among BBB-crossing AAV9 variants, suggesting that this motif plays a similar role in LY6A binding in other variants.

Taken together, our results reveal that the conformation of the VR-VIII loop in rAAVs correlates with binding affinity toward AAVR. This suggests a strategy for modulating AAVR binding affinity by engineering a lysine lever interaction to control the flexibility of the loop and its steric hindrance with the PKD2 domain of AAVR. We also provide proof of principle for another possible strategy for modulating AAVR binding affinity: modifying the insertion loop length. Current neurotropic vectors such as PHP.eB rely on a murine receptor, LY6A, that is not found in higher vertebrates. Novel library-design strategies for engineering rAAVs with CNS-biased tropism such as those suggested by this study are therefore essential for realizing the full promise of CNS gene therapy.

## MATERIALS AND METHODS

### AAV vector production

All AAV capsids were expressed and purified as described in Challis et al.<sup>43</sup> 7-mer modified PHP.eB variant capsids (TLAV( $\times 2$ ), TLAV(-), TLAV to AGAG, and eB-flip) capsids were cloned into the AAV9 backbone using the Q5 Site-Directed Mutagenesis Kit (NEB). HEK293T cells were cultured in 150-mm dishes at 37°C with 5% CO<sub>2</sub> until they reached 80%–90% confluency and were triple transfected using polyethylenimine (PEI) with pHelper, a cargo plasmid containing the GFP reporter gene expressed from the ubiquitous CAG promoter, and a plasmid encoding one of the following capsids: AAV9, PHP.B, PHP.eB, TLAV( $\times 2$ ), TLAV(-), TLAV to AGAG, eB-flip, AAV1, and AAV1-PHP.B. Media were collected after 72 h and media and cells at 120 h. Media were cleared by centrifugation, and viral particles were collected by precipitation with 8% polyethylene glycol (PEG) 8000 (Sigma-Aldrich). Cell pellets were lysed with salt-active nuclease (SAN) (ArticZymes). Precipitated viruses and lysate were combined and cleared by centrifugation. Viral particles in clarified supernatant were purified by ultracentrifugation in an iodixanol gradient. Viruses were concentrated and buffer exchanged into Dulbecco's phosphate-buffered saline (DPBS) (Thermo Fisher Scientific). Viruses were titered by measuring capsid protection of the WPRE cargo region using qPCR. Linearized cargo plasmid was used as a standard.

### Cryo-EM data collection and image processing

Three  $\mu\text{L}$  PHP.eB at a concentration of 8E13 vg/mL in DPBS was loaded onto glow-discharged Quantifoil R1.2/1.3/300 Cu EM grids and plunge frozen using a Vitrobot Mark IV (FEI). All cryo-EM was done in the Beckman Institute Resource Center for Transmission Electron Microscopy at Caltech, using a 200-keV Talos Arctica (Thermo Fisher Scientific) equipped with a K3 direct detector (Gatan). A total of 1,485 micrographs were collected, with 40 frames per movie, at a pixel size of 0.4345 Å/pixel (super res) and a total dose of 60 e<sup>-</sup>/Å<sup>2</sup>.

For the I1 symmetry structure, image-processing steps were performed in cryoSPARC (v.3.3.1).<sup>44</sup> Micrographs were motion corrected using the built-in patch motion correction function and binned to 0.869 Å/pixel. Contrast transfer function (CTF) estimation was performed with the built-in patch CTF estimation function. From 1,485 micrographs, a total of 81,327 particles were picked and subjected to one round of two-dimensional (2D) classification. From the 81,327 particles, 50,195 good-quality filled viral particles were selected for homogeneous refinement with I1 symmetry applied followed by global CTF refinement and local CTF refinement.<sup>45</sup> The final cryo-EM structure had a resolution of 2.24 Å as measured by the gold standard FSC at a cutoff of 0.143. The 3D model was built with Coot<sup>29</sup> and refined with the real-space refinement function implemented in PHENIX,<sup>28</sup> using a structure of AAV9 solved previously by X-ray crystallography (PDB: 3UX1) as an initial model.<sup>27</sup>

For the symmetry-free structure, image-processing steps were performed in Relion (v.3.1.3)<sup>46</sup> in the SBGrid software library.<sup>47</sup> Micrographs were motion corrected using MotionCorr<sup>48</sup> and binned to 0.869 Å/pixel. CTF estimation was performed with Gctf.<sup>49</sup> From 1,485 micrographs, a total of 97,560 particles were picked and subjected to two rounds of 2D classifications and one round of 3D classification. From the 97,560 particles, 49,405 good-quality full viral particles were selected for 3D auto-refinement followed by CTF refinement, Bayesian polishing, and post-processing. No symmetry was imposed, to enhance visualization of asymmetric features. The final cryo-EM structure had a resolution of 2.90 Å as measured by the gold standard FSC at a cutoff of 0.143.

All structure figures were created using Chimera.<sup>50</sup>

### RosettaRemodel structure prediction

Missing loop structures were modeled with RosettaRemodel (bundle release 2018.48.60516)<sup>31</sup> using a previously published model of PHP.B (PHP.B, PDB: 7RK8)<sup>30</sup> and our new PHP.eB atomic model, with a symmetrical input that considers interactions around the 3-fold axis. The template file in PDB format was first cleaned up with a Python script in the software bundle (tools/protein\_tools/scripts/clean\_pdb.py) to remove water molecules and comments in the file. A trimeric model was then built with PyMOL (v.2.3.3).<sup>51</sup> The trimer complex was saved as an individual .pdb file and then used to generate symmetry files. Symmetry files describing the C3 rotational symmetry were generated using a Perl script

(main/source/src/apps/public/symmetry/make\_symmdef\_file.pl, using NCS mode). The symmetry file and \_INPUT.pdb file generated from the Perl script were used as input files for the Remodel application. Flags for the remodel application were set to perform next-generation kinematic loop modeling.<sup>52</sup> The blueprint file was set to model the unresolved residues along with two flanking residues on each side. Due to their similar energy level scores, the top ten models of each variant were not ranked. Key settings in the flags and the blueprint file are listed in [Table S2](#).

### Phylogenetic tree generation

VP3 sequences of AAVs in the primate group (AAV1: residues 219–736; AAV2: residues 218–735; AAV3: residues 218–736; AAV4: residues 212–734; AAV5: residues 208–724; AAV6: residues 218–736; AAV7: residues 219–737; AAV8: residues 219–738; AAV9: residues 219–736; AAV10: residues 219–738; AAV11: residues 212–733; AAV12: residues 221–742; and AAV13: residues 217–733) were fed into the phylogenetic tree generator in phylogeny.fr and built-in programs applied.<sup>53</sup> Briefly, sequences were aligned with MUSCLE (v.3.8.31),<sup>54</sup> and ambiguous regions were eliminated by Gblocks (v.0.91b).<sup>55</sup> Using the cleaned-up alignment, a phylogenetic tree was generated using the PhyML (v.3.1/3.0 aLRT)<sup>56</sup> with 100 iterations of bootstrapping.

### Protein purification

Single PKD domains of AAVR (PKD1: residues 308–400; PKD2: residues 401–498; PKD3: residues 499–594; PKD4: residues 595–687; and PKD5: residues 688–781) were expressed as fusions double tagged with Myc and 6xHis in BL21 (DE3)-RIPL *E. coli*. The cells were lysed, and cell debris were cleared by centrifugation at 20,000 × *g* for 20 min. For each single domain, the resulting supernatant was loaded onto a Ni-NTA column (Qiagen) equilibrated with a buffer containing 50 mM Tris-HCl (pH 8.0), 100 mM NaCl, and 20 mM imidazole. The column was then sequentially washed with 20 mM Tris-HCl (pH 8.0), 20 mM imidazole, and a gradient of NaCl concentrations (500, 1,000, 500, and 150 mM) to remove non-specifically bound material. PKD domains were eluted using 20 mM Tris-HCl (pH 8.0) and 100 mM NaCl with a stepped imidazole gradient (50, 100, 150, and 250 mM), and the 250 mM imidazole fractions were used for experiments.

LY6A (residues 1–109) from C57BL/6 mice triple tagged with Fc (human IgG1), Myc, and 6xHis was transfected into HEK293T cells at 80%–90% confluency using PEI. Media containing secreted His-Fc-LY6A were collected after 120 h and filtered using a 0.22- $\mu$ m PES vacuum filter (Sigma-Millipore). His-Fc-LY6A in clarified media was captured with Ni-NTA resin (Qiagen) and eluted with 100 mM NaCl, 50 mM Tris-HCl (pH 8.0), and 150 mM imidazole. Purified His-Fc-LY6A was concentrated using a 10K Amicon concentrator (Sigma-Millipore).

### Pull-down assays

Prey rAAVs (0.01–0.05 pmol) were mixed with 6xHis-tagged bait, either purified AAVR single domains (ranging from 5–80 pmol, de-

pending on the purpose of the assay), His-Fc-LY6A (10–60 pmol), or His-Fc (30–60 pmol, negative control) and 15  $\mu$ L Ni-NTA resin in a buffer containing 50 mM Tris-HCl (pH 8.0), 100 mM NaCl, and 20 mM imidazole for 1 h at 4°C in a rotary shaker. The mixture was loaded onto a spin column and washed twice with 100  $\mu$ L (10 column volumes total) wash buffer containing 50 mM Tris-HCl (pH 8.0), 100 mM NaCl, and 20 mM imidazole to remove unbound rAAVs. Prey rAAVs interacting with the 6xHis-tagged bait were eluted with 80  $\mu$ L elution buffer containing 50 mM Tris-HCl (pH 8.0), 100 mM NaCl, and 150 mM imidazole. The resulting eluate was electrophoresed by SDS-PAGE and analyzed by western blotting with anti-VP1/VP2/VP3 and anti-6xHis antibodies. Western blot images were analyzed using ImageJ.<sup>57</sup>

### Amino acid frequency plot generation

The amino acid frequency plot of insertion loops of BBB-crossing AAV9 variants were created using Weblogo (v. 2.8.2).<sup>58</sup>

### Data availability statement

Cryo-EM map and 3D coordinates are available in wwPDB and EMDB with the following accession codes: I1 symmetry applied AAV-PHP.eB, PDB: 7UD4 and EMD: 26453 and symmetry-free AAV-PHP.eB, EMD: 26417.

### SUPPLEMENTAL INFORMATION

Supplemental information can be found online at <https://doi.org/10.1016/j.omtm.2022.07.011>.

### ACKNOWLEDGMENTS

We sincerely thank the staff of the Caltech CLARITY, Optogenetics, & Vector Engineering Center (CLOVER), and members of the Gradi-naru lab, especially Josette Medicielo and Zhe Qu, for their help with virus purification, and Catherine Oikonomou for help editing the manuscript. Cryo-EM was done in the Beckman Institute Resource Center for Transmission Electron Microscopy at Caltech. We especially thank Songye Chen for assisting with cryo-EM data collection. We are grateful to all members of phylogeny.fr and particularly Sebastian Santini (CNRS/AMU IGS UMR7256) and the PACA BioInfo platform (supported by IBiSA) for the availability and management of phylogeny.fr. This work is supported by a grant from the National Institutes of Health (NIH) to V.G. (NIH Pioneer DP1OD025535). [Figure 3A](#) was created with [BioRender.com](#).

### AUTHOR CONTRIBUTIONS

S.J., T.F.M., and V.G. conceived the idea, and V.G. supervised this project. S.J. determined the cryo-EM structures. S.J. and H.K.S. purified the capsids and proteins. S.J. and H.K.S. conducted the pull-down assays. X.D. conducted the RosettaRemodel prediction. S.J., T.F.M., and V.G. wrote the manuscript, and all authors reviewed the data and manuscript.

### DECLARATIONS OF INTERESTS

The authors declare no competing interests.

## REFERENCES

- Mietzsch, M., Péntzes, J.J., and Agbandje-McKenna, M. (2019). Twenty-five years of structural parvirology. *Viruses* 11, 362.
- Zinn, E., and Vandenberghe, L.H. (2014). Adeno-associated virus: fit to serve. *Curr. Opin. Virol.* 8, 90–97.
- Hermonat, P.L., and Muzyczka, N. (1984). Use of adeno-associated virus as a mammalian DNA cloning vector: transduction of neomycin resistance into mammalian tissue culture cells. *Proc. Natl. Acad. Sci. USA* 81, 6466–6470.
- Flotte, T.R. (2004). Gene therapy progress and prospects: recombinant adeno-associated virus (rAAV) vectors. *Gene Ther.* 11, 805–810.
- Wang, D., Tai, P.W.L., and Gao, G. (2019). Adeno-associated virus vector as a platform for gene therapy delivery. *Nat. Rev. Drug Discov.* 18, 358–378.
- Foust, K.D., Nurre, E., Montgomery, C.L., Hernandez, A., Chan, C.M., and Kaspar, B.K. (2009). Intravascular AAV9 preferentially targets neonatal neurons and adult astrocytes. *Nat. Biotechnol.* 27, 59–65.
- Manfredsson, F.P., Rising, A.C., and Mandel, R.J. (2009). AAV9: a potential blood-brain barrier buster. *Mol. Ther.* 17, 403–405.
- Deverman, B.E., Pravdo, P.L., Simpson, B.P., Kumar, S.R., Chan, K.Y., Banerjee, A., Wu, W.-L., Yang, B., Huber, N., Pasca, S.P., and Gradinaru, V. (2016). Cre-dependent selection yields AAV variants for widespread gene transfer to the adult brain. *Nat. Biotechnol.* 34, 204–209.
- Ravindra Kumar, S., Miles, T.F., Chen, X., Brown, D., Dobrev, T., Huang, Q., Ding, X., Luo, Y., Einarsson, P.H., Greenbaum, A., et al. (2020). Multiplexed Cre-dependent selection yields systemic AAVs for targeting distinct brain cell types. *Nat. Methods* 17, 541–550.
- Bedbrook, C.N., Deverman, B.E., and Gradinaru, V. (2018). Viral strategies for targeting the central and peripheral nervous systems. *Annu. Rev. Neurosci.* 41, 323–348.
- Chan, K.Y., Jang, M.J., Yoo, B.B., Greenbaum, A., Ravi, N., Wu, W.-L., Sánchez-Guardado, L., Lois, C., Mazmanian, S.K., Deverman, B.E., and Gradinaru, V. (2017). Engineered AAVs for efficient noninvasive gene delivery to the central and peripheral nervous systems. *Nat. Neurosci.* 20, 1172–1179.
- Shen, S., Bryant, K.D., Brown, S.M., Randell, S.H., and Asokan, A. (2011). Terminal N-linked galactose is the primary receptor for adeno-associated virus 9. *J. Biol. Chem.* 286, 13532–13540.
- Bell, C.L., Vandenberghe, L.H., Bell, P., Limberis, M.P., Gao, G.-P., Van Vliet, K., Agbandje-McKenna, M., and Wilson, J.M. (2011). The AAV9 receptor and its modification to improve in vivo lung gene transfer in mice. *J. Clin. Invest.* 121, 2427–2435.
- Mietzsch, M., Broecker, F., Reinhardt, A., Seeberger, P.H., and Heilbronn, R. (2014). Differential adeno-associated virus serotype-specific interaction patterns with synthetic heparins and other glycans. *J. Virol.* 88, 2991–3003.
- Péntzes, J.J., Chipman, P., Bhattacharya, N., Zeher, A., Huang, R., McKenna, R., and Agbandje-McKenna, M. (2021). Adeno-associated virus 9 structural rearrangements induced by endosomal trafficking pH and glycan attachment. *J. Virol.* 95, e0084321.
- Pillay, S., Meyer, N.L., Puschnik, A.S., Davulcu, O., Diep, J., Ishikawa, Y., Jae, L.T., Wosen, J.E., Nagamine, C.M., Chapman, M.S., and Carette, J.E. (2016). An essential receptor for adeno-associated virus infection. *Nature* 530, 108–112.
- Summerford, C., Johnson, J.S., and Samulski, R.J. (2016). AAVR: a multi-serotype receptor for AAV. *Mol. Ther.* 24, 663–666.
- Dudek, A.M., Pillay, S., Puschnik, A.S., Nagamine, C.M., Cheng, F., Qiu, J., Carette, J.E., and Vandenberghe, L.H. (2018). An alternate route for adeno-associated virus (AAV) entry independent of AAV receptor. *J. Virol.* 92, e02213–17.
- Pillay, S., Zou, W., Cheng, F., Puschnik, A.S., Meyer, N.L., Ganaie, S.S., Deng, X., Wosen, J.E., Davulcu, O., Yan, Z., et al. (2017). Adeno-associated virus (AAV) serotypes have distinctive interactions with domains of the cellular AAV receptor. *J. Virol.* 91, e00391–17.
- Zhang, R., Xu, G., Cao, L., Sun, Z., He, Y., Cui, M., Sun, Y., Li, S., Li, H., Qin, L., et al. (2019). Divergent engagements between adeno-associated viruses with their cellular receptor AAVR. *Nat. Commun.* 10, 3760.
- Zhang, R., Cao, L., Cui, M., Sun, Z., Hu, M., Zhang, R., Stuart, W., Zhao, X., Yang, Z., Li, X., et al. (2019). Adeno-associated virus 2 bound to its cellular receptor AAVR. *Nat. Microbiol.* 4, 675–682.
- Meyer, N.L., Hu, G., Davulcu, O., Xie, Q., Noble, A.J., Yoshioka, C., Gingerich, D.S., Trzynka, A., David, L., Stagg, S.M., and Chapman, M.S. (2019). Structure of the gene therapy vector, adeno-associated virus with its cell receptor, AAVR. *Elife* 8, e44707.
- Silveria, M.A., Large, E.E., Zane, G.M., White, T.A., and Chapman, M.S. (2020). The structure of an AAV5-AAVR complex at 2.5 Å resolution: implications for cellular entry and immune neutralization of AAV gene therapy vectors. *Viruses* 12, 1326.
- Huang, Q., Chan, K.Y., Tobey, I.G., Chan, Y.A., Poterba, T., Boutros, C.L., Balazs, A.B., Daneman, R., Bloom, J.M., Seed, C., and Deverman, B.E. (2019). Delivering genes across the blood-brain barrier: LY6A, a novel cellular receptor for AAV-PHP.B capsids. *PLoS One* 14, e0225206.
- Batista, A.R., King, O.D., Reardon, C.P., Davis, C., Shankaracharya, Philip, V., Gray-Edwards, H., Aronin, N., Lutz, C., Landers, J., and Sena-Estevés, M. (2020). Ly6a differential expression in blood-brain barrier is responsible for strain specific central nervous system transduction profile of AAV-PHP. *Hum. Gene Ther.* 31, 90–102.
- Hordeaux, J., Yuan, Y., Clark, P.M., Wang, Q., Martino, R.A., Sims, J.J., Bell, P., Raymond, A., Stanford, W.L., and Wilson, J.M. (2019). The GPI-linked protein LY6A drives AAV-PHP.B transport across the blood-brain barrier. *Mol. Ther.* 27, 912–921.
- DiMattia, M.A., Nam, H.-J., Van Vliet, K., Mitchell, M., Bennett, A., Gurda, B.L., McKenna, R., Olson, N.H., Sinkovits, R.S., Potter, M., et al. (2012). Structural insight into the unique properties of adeno-associated virus serotype 9. *J. Virol.* 86, 6947–6958.
- Liebschner, D., Afonine, P.V., Baker, M.L., Bunkóczi, G., Chen, V.B., Croll, T.I., Hintze, B., Hung, L.-W., Jain, S., McCoy, A.J., et al. (2019). Macromolecular structure determination using X-rays, neutrons and electrons: recent developments in Phenix. *Acta Crystallogr. D Struct. Biol.* 75, 861–877.
- Emsley, P., Lohkamp, B., Scott, W.G., and Cowtan, K. (2010). Features and development of coot. *Acta Crystallogr. D Biol. Crystallogr.* 66, 486–501.
- Martino, R.A., Fluck, E.C., Murphy, J., Wang, Q., Hoff, H., Pumroy, R.A., Lee, C.Y., Sims, J.J., Roy, S., Moiseenkova-Bell, V.Y., and Wilson, J.M. (2021). Context-Specific function of the engineered peptide domain of PHP. *J. Virol.* 95, e0116421.
- Huang, P.-S., Ban, Y.-E.A., Richter, F., Andre, I., Vernon, R., Schief, W.R., and Baker, D. (2011). RosettaRemodel: a generalized framework for flexible backbone protein design. *PLoS One* 6, e24109.
- Allen, W.E., Kauvar, I.V., Chen, M.Z., Richman, E.B., Yang, S.J., Chan, K., Gradinaru, V., Deverman, B.E., Luo, L., and Deisseroth, K. (2017). Global representations of goal-directed behavior in distinct cell types of mouse neocortex. *Neuron* 94, 891–907.e6.
- Robinson, J.E., Coughlin, G.M., Hori, A.M., Cho, J.R., Mackey, E.D., Turan, Z., Patriarchi, T., Tian, L., and Gradinaru, V. (2019). Optical dopamine monitoring with dLight1 reveals mesolimbic phenotypes in a mouse model of neurofibromatosis type 1. *Elife* 8, e48983.
- Bedbrook, C.N., Yang, K.K., Robinson, J.E., Mackey, E.D., Gradinaru, V., and Arnold, F.H. (2019). Machine learning-guided channelrhodopsin engineering enables minimally-invasive optogenetics. *Nat. Methods* 16, 1176–1184.
- Helseth, A.R., Hernandez-Martinez, R., Hall, V.L., Oliver, M.L., Turner, B.D., Caffall, Z.F., Rittiner, J.E., Shipman, M.K., King, C.S., Gradinaru, V., et al. (2021). Cholinergic neurons engage the integrated stress response for dopamine modulation and skill learning. *Science* 372, eabe1931.
- Nagai, J., Bellafard, A., Qu, Z., Yu, X., Ollivier, M., Gangwani, M.R., Diaz-Castro, B., Coppola, G., Schumacher, S.M., Golshani, P., et al. (2021). Specific and behaviorally consequential astrocyte Gq GPCR signaling attenuation in vivo with iBARK. *Neuron* 109, 2256–2274.e9.
- Morabito, G., Giannelli, S.G., Ordazzo, G., Bido, S., Castoldi, V., Indrigo, M., Cabassi, T., Cattaneo, S., Luoni, M., Cancellieri, C., et al. (2017). AAV-PHP.B-Mediated global-scale expression in the mouse nervous system enables GBA1 gene therapy for wide protection from synucleinopathy. *Mol. Ther.* 25, 2727–2742.
- Challis, C., Hori, A., Sampson, T.R., Yoo, B.B., Challis, R.C., Hamilton, A.M., Mazmanian, S.K., Volpicelli-Daley, L.A., and Gradinaru, V. (2020). Gut-seeded  $\alpha$ -synuclein fibrils promote gut dysfunction and brain pathology specifically in aged mice. *Nat. Neurosci.* 23, 327–336.
- Rauch, J.N., Luna, G., Guzman, E., Audouard, M., Challis, C., Sibih, Y.E., Leshuk, C., Hernandez, I., Wegmann, S., Hyman, B.T., et al. (2020). LRP1 is a master regulator of tau uptake and spread. *Nature* 580, 381–385.

40. Luoni, M., Giannelli, S., Indrigo, M.T., Niro, A., Massimino, L., Iannielli, A., Passeri, L., Russo, F., Morabito, G., Calamita, P., et al. (2020). Whole brain delivery of an instability-prone *Mecp2* transgene improves behavioral and molecular pathological defects in mouse models of Rett syndrome. *Elife* 9, e52629.
41. Duan, Y., Ye, T., Qu, Z., Chen, Y., Miranda, A., Zhou, X., Lok, K.-C., Chen, Y., Fu, A.K.Y., Gradinaru, V., and Ip, N.Y. (2022). Brain-wide Cas9-mediated cleavage of a gene causing familial Alzheimer's disease alleviates amyloid-related pathologies in mice. *Nat. Biomed. Eng.* 6, 168–180.
42. Monteys, A.M., Hundley, A.A., Ranum, P.T., Tecedor, L., Muehlmann, A., Lim, E., Lukashev, D., Sivasankaran, R., and Davidson, B.L. (2021). Regulated control of gene therapies by drug-induced splicing. *Nature* 596, 291–295.
43. Challis, R.C., Ravindra Kumar, S., Chan, K.Y., Challis, C., Beadle, K., Jang, M.J., Kim, H.M., Rajendran, P.S., Tompkins, J.D., Shivkumar, K., et al. (2019). Systemic AAV vectors for widespread and targeted gene delivery in rodents. *Nat. Protoc.* 14, 379–414.
44. Punjani, A., Rubinstein, J.L., Fleet, D.J., and Brubaker, M.A. (2017). cryoSPARC: algorithms for rapid unsupervised cryo-EM structure determination. *Nat. Methods* 14, 290–296.
45. Zivanov, J., Nakane, T., and Scheres, S.H.W. (2020). Estimation of high-order aberrations and anisotropic magnification from cryo-EM data sets in RELION-3.1. *IUCr* 7, 253–267.
46. Zivanov, J., Nakane, T., Forsberg, B.O., Kimanius, D., Hagen, W.J., Lindahl, E., and Scheres, S.H. (2018). New tools for automated high-resolution cryo-EM structure determination in RELION-3. *Elife* 7, e42166.
47. Morin, A., Eisenbraun, B., Key, J., Sanschagrin, P.C., Timony, M.A., Ottaviano, M., and Sliz, P. (2013). Collaboration gets the most out of software. *Elife* 2, e01456.
48. Zheng, S.Q., Palovcak, E., Armache, J.-P., Verba, K.A., Cheng, Y., and Agard, D.A. (2017). MotionCor2: anisotropic correction of beam-induced motion for improved cryo-electron microscopy. *Nat. Methods* 14, 331–332.
49. Zhang, K. (2016). Gctf: real-time CTF determination and correction. *J. Struct. Biol.* 193, 1–12.
50. Goddard, T.D., Huang, C.C., Meng, E.C., Pettersen, E.F., Couch, G.S., Morris, J.H., and Ferrin, T.E. (2018). UCSF ChimeraX: meeting modern challenges in visualization and analysis. *Protein Sci.* 27, 14–25.
51. Schrödinger, L.L.C. (2022). The PyMOL Molecular Graphics System. Version 2.3.3. <https://pymol.org/>.
52. Stein, A., and Kortemme, T. (2013). Improvements to robotics-inspired conformational sampling in rosetta. *PLoS One* 8, e63090.
53. Dereeper, A., Guignon, V., Blanc, G., Audic, S., Buffet, S., Chevenet, F., Dufayard, J.-F., Guindon, S., Lefort, V., Lescot, M., et al. (2008). Phylogeny.fr: robust phylogenetic analysis for the non-specialist. *Nucleic Acids Res.* 36, W465–W469.
54. Edgar, R.C. (2004). MUSCLE: multiple sequence alignment with high accuracy and high throughput. *Nucleic Acids Res.* 32, 1792–1797.
55. Castresana, J. (2000). Selection of conserved blocks from multiple alignments for their use in phylogenetic analysis. *Mol. Biol. Evol.* 17, 540–552.
56. Guindon, S., Dufayard, J.-F., Lefort, V., Anisimova, M., Hordijk, W., and Gascuel, O. (2010). New algorithms and methods to estimate maximum-likelihood phylogenies: assessing the performance of PhyML 3.0. *Syst. Biol.* 59, 307–321.
57. Schneider, C.A., Rasband, W.S., and Eliceiri, K.W. (2012). NIH Image to ImageJ: 25 years of image analysis. *Nat. Methods* 9, 671–675.
58. Crooks, G.E., Hon, G., Chandonia, J.-M., and Brenner, S.E. (2004). WebLogo: a sequence logo generator. *Genome Res* 14, 1188–1190.